

Large Eddy Simulation of Turbulent Channel Flow at $Re_\tau = 590$

M. Saiful Islam Mallik^{1,2}, M. Ashraf Uddin¹ and M. Ashaque Meah¹

¹Department of Mathematics, Shahjalal University of Science & Technology, Sylhet, Bangladesh.

²Department of Arts and Sciences, Ahsanullah University of Science & Technology, Dhaka, Bangladesh.

Abstract: A large eddy simulation of a plane turbulent channel flow is performed by using the third order Low-Storage Runge-Kutta method in time and second order Finite Difference formulation in space with staggered grid at a Reynolds number 590 based on the channel half width and wall shear velocity. The computation is performed in a domain where streamwise and spanwise directions are periodic with $32 \times 64 \times 32$ grid points. Standard Smagorinsky model is used for subgrid scale modeling. Turbulence statistics of this simulation are compared with Direct Numerical Simulation (DNS) data. The behavior of the flow structures in the computed flow field have also been discussed.

Keywords: Large eddy simulation, staggered grid, turbulent channel flow.

I. Introduction

Turbulent channel flow has been studied extensively to increase the understanding of the mechanics of wall-bounded turbulent flows. Its geometric simplicity is attractive for both experimental and theoretical investigations of complex turbulence interactions near a wall. As a result, a large number of experimental and computational studies of channel flow have been carried out [1-6].

During the past decades, Large Eddy Simulation (LES) has been demonstrated to be a useful research tool for understanding the physics of turbulence than DNS. With the development of the technique of numerical simulation, Large-Eddy Simulation has begun to be applied to industrial flows, such as flow in a turbomachine. LES is less expensive and can simulate very complex flow fields in turbulence. In LES method, large-scale motion is exactly calculated and the effects of subgrid-scale (SGS) motions on the evolution of large scales, which is expected to be universal is modeled. Discretization method is another issue to conduct LES in turbulence [5-8]. A literature review suggests that the numerical method widely used for spatial discretization in LES is the conventional finite difference method with structured grids [9-10].

Explicit Runge-Kutta methods are a popular choice for the time discretization of the Navier-Stokes equations. Compared with (explicit) multi-step methods, Runge-Kutta methods have in general better stability properties, do not have a start-up problem, and easily allow for adaptive time stepping, although they generally require the solution to a Poisson equation for the pressure at each stage of the Runge-Kutta method. The application of explicit Runge-Kutta methods to the incompressible Navier-Stokes equations is not straight forward because of the differential-algebraic nature of the equations. It is common practice to explicitly advance the velocity at each stage as if the discretized equations are a system of ordinary differential equations, and subsequently solve a Poisson equation for the pressure to make the velocity field divergence-free [11].

To simulate the turbulent channel flow it is necessary to do sufficiently long time integration in LES that need much wider computation region, applying a low storage scheme is significant to make sufficient utilization of computer resource. Low-storage Runge-Kutta schemes require minimum levels of memory locations during the time integration and efficiently comply with the modern large-scale scientific computing needs. A number of explicit low-storage Runge-Kutta schemes of third-order accuracy were derived by Williamson [12].

The aim of our present research is to perform LES of a plane turbulent channel flow. Spatial and temporal discretization has been done using the third order Low-Storage Runge-Kutta method and second order finite difference formulation respectively with staggered grid. The computational domain is $2\pi\delta \times 2\delta \times \pi\delta$ where the grid spacings in the streamwise and spanwise directions are uniform while the wall normal grid distribution is non-uniform with a hyperbolic-tangent type stretching function. Essential turbulence statistics of the flow field are computed and compared with DNS data of Moser et al. [2]. Contours of instantaneous streamwise velocity distribution at the centerline of the channel and streamwise shear velocity distribution at the immediate vicinity of the wall have also been discussed. Iso-surfaces of the second invariant ($Q = 5$) of velocity gradient tensor in the turbulent channel flow are visualized.

II. Governing Equations

The governing equations of LES for an incompressible plane channel flow are the filtered Navier-Stokes and continuity equations for constant density in Cartesian co-ordinates given as

$$\frac{\partial \bar{u}_i}{\partial t} + \frac{\partial}{\partial x_j} (\overline{u_i u_j}) = -\frac{1}{\rho} \frac{\partial \bar{p}}{\partial x_i} + \frac{\partial}{\partial x_j} \left[\nu_e \left(\frac{\partial \bar{u}_i}{\partial x_j} + \frac{\partial \bar{u}_j}{\partial x_i} \right) \right], \text{ where } i, j = 1, 2, 3 \quad (1)$$

$$\frac{\partial \bar{u}_i}{\partial x_i} = 0 \quad (2)$$

where the index $i = 1, 2, 3$ refers to the x, y and z directions respectively. Here $\bar{u}_x, \bar{u}_y, \bar{u}_z$ are streamwise, wall normal and spanwise filtered velocity respectively. \bar{p} is the filtered pressure and ν_e is the total viscosity (equal to the sum of the molecular and SGS eddy viscosity, $\nu + \nu_s$). A schematic geometry of the plane turbulent channel flow and the co-ordinate system are shown in Fig. 1. The equations are non-dimensionalized by the channel half-width δ , and the wall shear velocity u_τ . The Reynolds number is therefore written as $Re = u_\tau \delta / \nu$.

In LES, the velocity field u_i is decomposed into a large scale component \bar{u}_i and a subgrid scale component u'_i by applying a spatial filtering operation. The resolved velocity component \bar{u}_i can be expressed as follows:

$$\bar{u}_i(x_1, x_2, x_3, t) = \int_{-\infty}^{+\infty} \int_{-\infty}^{+\infty} \int_{-\infty}^{+\infty} \left(\prod_{i=1}^3 G_i(x_i - x'_i) \right) u_i(x'_1, x'_2, x'_3, t) dx'_1 dx'_2 dx'_3 \quad (3)$$

where $G_i(x_i - x'_i)$ is a general filtering function which satisfies the following relation:

$$\int_{-\infty}^{+\infty} \int_{-\infty}^{+\infty} \int_{-\infty}^{+\infty} \left(\prod_{i=1}^3 G_i(x_i - x'_i) \right) dx'_1 dx'_2 dx'_3 = 1 \quad (4)$$

Since the continuity equation is linear, filtering does not change it significantly. However, it is important to note that $\overline{u_i u_j} \neq \bar{u}_i \cdot \bar{u}_j$, and the quantity on the left side of the inequality cannot be easily computed. So, a modeling approximation for the difference between the two sides of this inequality,

$$\tau_{ij}^s = \overline{u_i u_j} - \bar{u}_i \cdot \bar{u}_j \quad (5)$$

must be needed. τ_{ij}^s is called the subgrid scale (SGS) Reynolds stress, which is in fact the large scale momentum flux caused by the action of the small or unresolved scales. The models used to approximate the SGS Reynolds stress are called subgrid scale (SGS) models. The most commonly used subgrid scale model is the Smagorinsky model. This model represents the SGS eddy viscosity according to

$$\nu_s = (C_S \cdot \Delta)^2 |\bar{S}|. \quad (6)$$

Here C_S is the Smagorinsky constant whose value is taken to be 0.065 [4], $\Delta = (\Delta x \Delta y \Delta z)^{1/3}$ is filter width

and $|\bar{S}| = \sqrt{2 \bar{S}_{ij} \bar{S}_{ij}}$ is the magnitude of strain rate, where $\bar{S}_{ij} = \frac{1}{2} \left(\frac{\partial \bar{u}_i}{\partial x_j} + \frac{\partial \bar{u}_j}{\partial x_i} \right)$. To reduce the near-wall eddy

viscosity for the wall bounded flows the SGS eddy viscosity can be modified as:

$$\nu_s = (C_S \cdot f_S \cdot \Delta)^2 |\bar{S}|. \quad (7)$$

Here $f_S = 1 - \exp\left(-\frac{y^+}{A^+}\right)$ is the Van-Driest damping function, where y^+ is the distance from the wall in viscous

wall units defined as $y^+ = \frac{y u_\tau}{\nu}$ and A^+ is a constant usually taken to be approximately 25 [13].

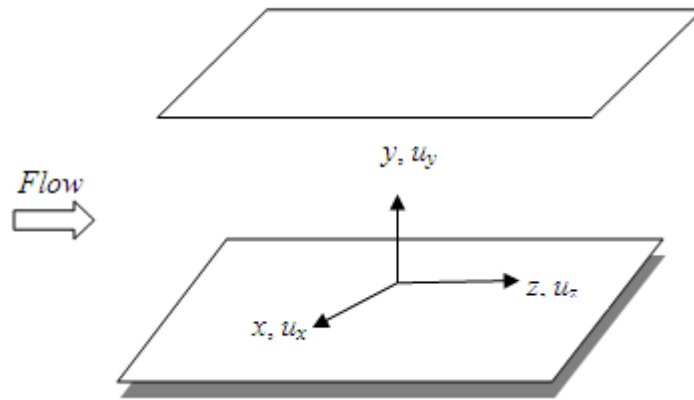


Fig. 1: Schematic geometry of plane channel flow.

III. Numerical Method

The governing equations of LES are solved using the third order low-storage explicit Runge-Kutta method in time [14] and the second order finite difference formulation in space. The coupling between continuity equation and pressure fields is performed by the simplified marker-and-cell (SMAC) method [15]. Poisson equation is solved iteratively by a Preconditioned Incomplete Cholesky Decomposition Conjugated Gradient method. In the following subsections, staggered grid arrangement, discrete and interpolation operators are shortly introduced.

III.I. Staggered grid arrangement

Staggered grids may be constructed by several methods. An example of a staggered grid system in a two-dimensional plane is shown in Fig. 2. On the staggered grid, scalar variable pressure are stored at the nodes (intersection point of two lines) and velocities are defined at the middle of the two nodes. Horizontal (\rightarrow) arrows indicate the locations for u_x – velocities and vertical (\uparrow) ones denote those for u_y – velocities. The continuity is centered at pressure points. The momentum equation corresponding to each velocity component is centered at the respective velocity point [16]. The biggest advantage of the staggered arrangement is the strong coupling between the velocities and the pressure.

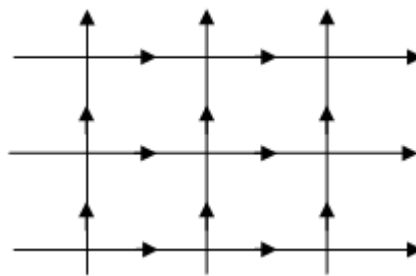


Fig. 2: Staggered grid system.

In this study, the grid spacings in the periodic directions are uniform. The wall normal grid is stretched by using a hyperbolic-tangent type stretching function [16]

$$Y(j) = \frac{\tanh\left[\gamma\left(\frac{2j}{N} - 1\right)\right]}{\tanh(\gamma)}, \quad j = 0, 1, \dots, N, \quad (8)$$

where the stretching parameter, γ is taken to be 2.25. We use both uniform and stretched grids and maintain the order of accuracy is unaltered.

III.II. Discrete Operators

There are a variety of discretization techniques available for developing discrete approximations to a set of governing partial differential equations such as Navier-Stokes equations. Let the finite difference operator with

stencil size 1 acting on a discrete variable φ with respect to x for structural Cartesian meshes with uniform spacing be defined as

$$\left. \frac{\partial_I \varphi}{\partial_I x} \right|_{i,j,k} = \frac{\varphi_{i,j,k} - \varphi_{i-1,j,k}}{\Delta x} \quad (9)$$

where the grid spacings Δx are constant in x direction, and (i, j, k) denotes associated mesh indices in x, y and z directions. Subscript “1” indices the stencil size. Discrete operators in the y and z – directions are similarly defined.

In addition to the discrete differencing operator we also define interpolation operators with stencil size 1 acting

on a variable u_x in the x – direction as $\left. \overline{u}_x^{Ix} \right|_{i,j,k}^L \equiv \frac{\overline{u}_x|_{i,j,k} + \overline{u}_x|_{i-1,j,k}}{2}$ and $\left. \overline{u}_x^{Ix} \right|_{i,j,k}^R \equiv \frac{\overline{u}_x|_{i,j,k} + \overline{u}_x|_{i+1,j,k}}{2}$,

where L and R indicate the approximation of $\left. \overline{u}_x^{1x} \right|_{i,j,k}$ to the one-half left and right of the grid (i, j, k) in x –

direction. The interpolation operator acting on the same variable \overline{u}_x in y and z – directions are similarly defined.

Interpolation operators acting on the other variables (\overline{u}_y and \overline{u}_z) associated to the directions are defined similarly as above where (i, j, k) denotes associated mesh indices in x, y and z directions.

IV. Computational Parameter and Grid Spacing

The computational domain of the mesh is selected to be $2\pi\delta \times 2\delta \times \pi\delta$ in streamwise, wall normal and spanwise directions respectively. The computation has been performed using $32 \times 64 \times 32$ computational grids and the possible Reynolds number, $Re_\tau = 590$ based on the channel half width, δ and wall shear velocity, u_τ . The computation has been done with non-dimensional time increment, $\Delta t = 0.002$, which maintained a CFL number,

$$CFL = \Delta t \max \left(\frac{|\overline{u}_x|}{\Delta x} + \frac{|\overline{u}_y|}{\Delta y} + \frac{|\overline{u}_z|}{\Delta z} \right) = 0.791 < 1.0. \text{ The computation is executed up to non-dimensional time, } t = n.$$

Δt , where n is the number of time step. With the computational domain, the grid spacings in the streamwise and spanwise directions are $\Delta x^+ \approx 116$ and $\Delta z^+ \approx 58$ wall units respectively. In the wall normal direction ($1 \leq y \leq +1$) the minimum grid spacing is $\Delta y^+ \approx 2$ wall unit which exist at the immediate vicinity of the wall and maximum grid spacing is $\Delta y^+ \approx 42$ wall unit which exist at the centerline of the channel. The first mesh point away from the wall is at $y^+ \approx 0.885$ wall unit. The superscript ‘+’ indicates a non-dimensional quantity scaled by the wall variables; e.g. $y^+ = y u_\tau / \nu$, where ν is the kinematic viscosity and $u_\tau = (\tau_w / \rho)^{1/2}$ is the wall shear velocity.

V. Boundary Conditions

We consider fully developed incompressible viscous flow and make use of periodic boundary conditions in the streamwise and spanwise directions. For the staggered grid arrangement we set up additional nodes surrounding the physical boundary. The calculations are performed at internal nodes only. The wall boundary condition is no-slip. Just outside the solution domain the values of the velocity components are equated to the values of the nearest node just inside the solution domain [17]. The pressure boundary condition is periodic in the streamwise and spanwise directions. But in the wall normal direction the values of \overline{p} , just outside the solution domain, are determined by assuming a zero gradient [18].

VI. Temporal Schemes for LES in Plane Turbulent Channel Flow

Since the three components of the velocity vector, \mathbf{u} in the momentum equations are coupled with the pressure, \overline{p} through the continuity equation, these equations for the four variables ($\overline{u}_x, \overline{u}_y, \overline{u}_z, \overline{p}$) have to be solved at the same time. The temporal discretization used in our LES code for simulating the plane turbulent channel flow is the third order low storage explicit Runge-Kutta scheme which is applied for the nonlinear convection and the viscous terms. This scheme requires only two levels of memory locations during the time integration. Such a scheme reads the following sub-steps:

Sub-step 1:

$$\hat{u}_i^1 = \bar{u}_i^n + \alpha_1 \Delta t \overbrace{F_i(\bar{u}^n)}^{H_i^1} - \gamma_1 \frac{\Delta t}{\rho} \frac{\partial \bar{p}^n}{\partial x_i}$$

$$\frac{\partial \hat{u}_i^1}{\partial x_i} = 0$$

$$p^1 = \bar{p}^n - \psi^1$$

$$\bar{u}_i^1 = \hat{u}_i^1 + \gamma_1 \frac{\Delta t}{\rho} \frac{\partial \psi^1}{\partial x_i}$$

Sub-step 2:

$$\hat{u}_i^2 = \bar{u}_i^1 + \alpha_2 \Delta t \overbrace{F_i(\bar{u}^1)}^{H_i^2} + \beta_2 \Delta t H_i^1 - \gamma_2 \frac{\Delta t}{\rho} \frac{\partial p^1}{\partial x_i}$$

$$\frac{\partial \hat{u}_i^2}{\partial x_i} = 0$$

$$p^2 = p^1 - \psi^2$$

$$\bar{u}_i^2 = \hat{u}_i^2 + \gamma_2 \frac{\Delta t}{\rho} \frac{\partial \psi^2}{\partial x_i}$$

Sub-step 3:

$$\hat{u}_i^3 = \bar{u}_i^2 + \alpha_3 \Delta t F_i(\bar{u}^2) + \beta_3 \Delta t H_i^2 - \gamma_3 \frac{\Delta t}{\rho} \frac{\partial p^2}{\partial x_i}$$

$$\frac{\partial \hat{u}_i^3}{\partial x_i} = 0$$

$$p^3 = p^2 - \psi^3$$

$$\bar{u}_i^3 = \hat{u}_i^3 + \gamma_3 \frac{\Delta t}{\rho} \frac{\partial \psi^3}{\partial x_i}$$

where F_i ($i = x, y, z$) are the convective and viscous terms and \bar{u}_i ($i = x, y, z$) are the velocity components. n is the level of time. The superscripts 1, 2, 3 on the variables represent the sub-step number. First equation of every sub-step is the momentum equation. Second equation is the Poisson equation for pressure. After the Poisson equation have been solved, pressure potential, ψ is found. The pressure potential is then used to calculate the pressure, \bar{p} and velocity components from third and fourth equations respectively of every sub-step. Final solutions $(\bar{u}_x, \bar{u}_y, \bar{u}_z, \bar{p})$ for every level of time are found from sub-step 3. Boundary conditions are assigned at every sub-step k . The values of α_k , β_k and γ_k are shown below:

$$\begin{array}{lll} \alpha_1 = \frac{8}{15} & \beta_1 = 0 & \gamma_1 = \frac{4}{15} \\ \alpha_2 = \frac{5}{12} & \beta_2 = -\frac{17}{60} & \gamma_2 = \frac{1}{15} \\ \alpha_3 = \frac{3}{4} & \beta_3 = -\frac{5}{12} & \gamma_3 = \frac{1}{6} \end{array}$$

VII. Results and Discussions

VII.I. Turbulence Statistics

In this section we discuss some statistics of the computed flow field in 3D turbulent channel flow. The computed results are compared with the DNS data obtained by Moser et al. [2]. Simulations are initialized with a random solenoidal velocity field and integrated ahead in time with finite viscosity.

The profile of the mean velocity non-dimensional by the wall-shear velocity corresponding to the lower half of the channel is shown in Fig. 3, which is defined as

$$u_x^+ = \frac{\langle \bar{u}_x \rangle}{u_\tau} \tag{10}$$

The collapse of the mean velocity profile corresponding to the lower half of the channel is shown in this figure. Numerous experiments have shown that the near-wall region can be largely subdivided into three layers: viscous sub-layer ($y^+ \leq 5$), buffer layer ($5 < y^+ \leq 30$) and logarithmic inertial layer ($y^+ > 30$) [13]. From Fig.3 it can be observed that within the viscous sub-layer the DNS and LES mean velocity profiles are almost collapsed, but here after in the buffer layer the LES profiles are seen to be under predicted. Finally, in the logarithmic inertial layer the LES profiles over predict the DNS profile.

Fig. 4(a, b, c) show the DNS and LES profiles of root mean square (r.m.s.) of velocity components normalized by the wall shear velocity defined as

$$u_{x \text{ r.m.s.}}^+ = \sqrt{\langle u_x^2 \rangle - \langle u_x \rangle^2} / u_\tau \tag{11}$$

$$u_{y \text{ r.m.s.}}^+ = \sqrt{\langle u_y^2 \rangle - \langle u_y \rangle^2} / u_\tau \tag{12}$$

$$u_{z \text{ r.m.s.}}^+ = \sqrt{\langle u_z^2 \rangle - \langle u_z \rangle^2} / u_\tau \tag{13}$$

The profiles of streamwise root mean square velocity are displayed in Fig. 4(a). This figure reveals that in the viscous sub-layer the DNS and LES profiles are almost collapsed. After that the LES profiles are seen to be over predicted. Note that the peak value of the LES profile is about 3.8 which occurs at $y^+ \approx 20$. Beyond $y^+ \approx 20$ the trend of this profile is always decreasing until the end of the range. Although there exists a noticeable difference in the near wall region ($y^+ \approx 10 - 200$), away from the wall the computed profiles show a good agreement with the DNS profile obtained by Moser et al. [2]. The profiles of wall normal and spanwise root mean square velocity fields are shown in Fig. 4(b) and Fig. 4(c) respectively. In these figures the computed profiles of wall normal and spanwise root mean square velocity fields are seen to be under predicted in the whole calculation domain.

Fig. 5 presents the profile of non-dimensional Reynolds stress, $\frac{\overline{u'_x u'_y}}{u_\tau^2}$ corresponding to the channel half width. In a fully developed channel flow this profile is a straight line when the flow reaches an equilibrium state. The computed results clearly indicate that this is the case. It can be observed that at the near wall region ($y^+ \approx 0 - 100$) the LES profile under predicts the DNS profile. After that ($y^+ > 53$), there is hardly noticeable discrepancy between the DNS and LES profiles. Note that the peak in this profile occurs at $y^+ \approx 60$, which is well within the region for which the Reynolds number, $Re_\tau = 590$.

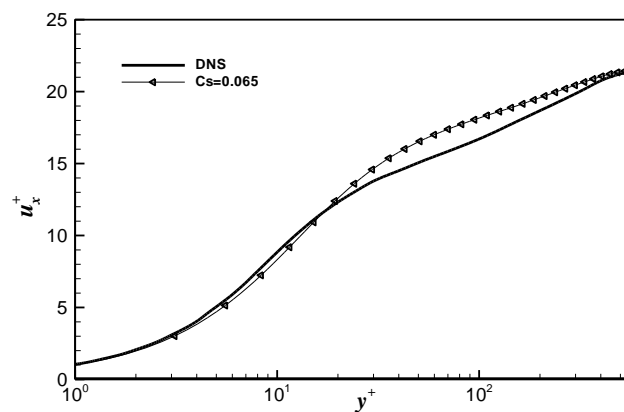


Fig. 3. Mean velocity profile in wall units.

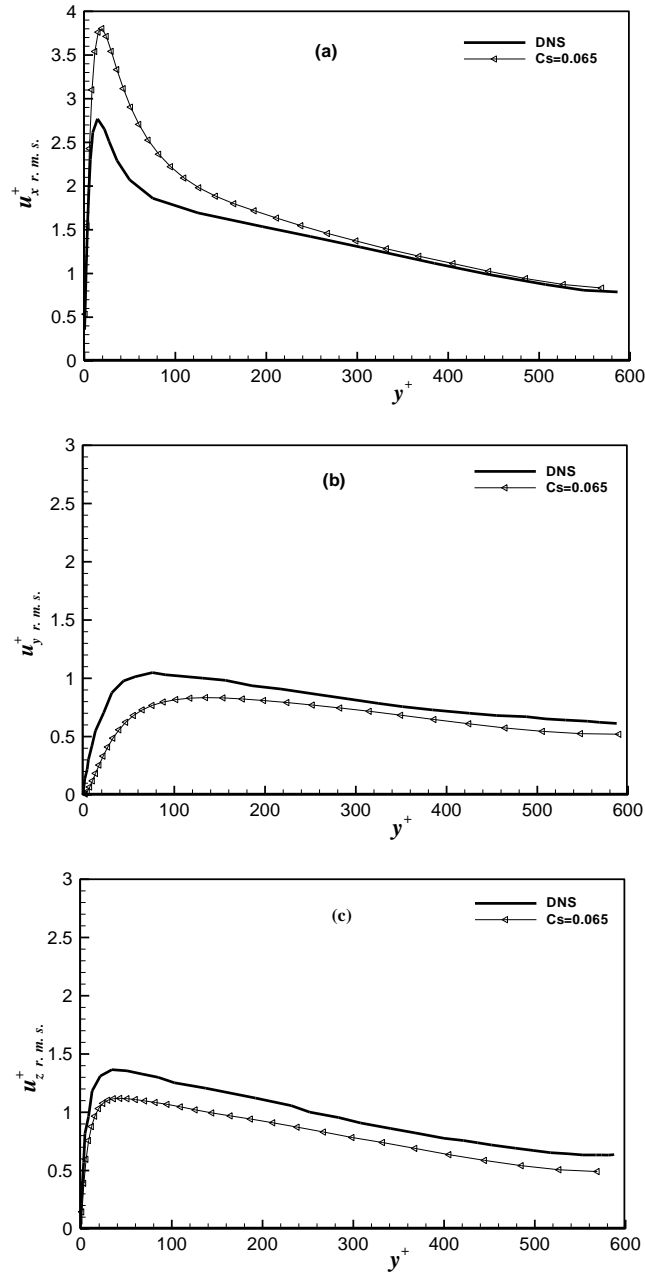


Fig. 4. Root mean square velocity profiles in wall units.

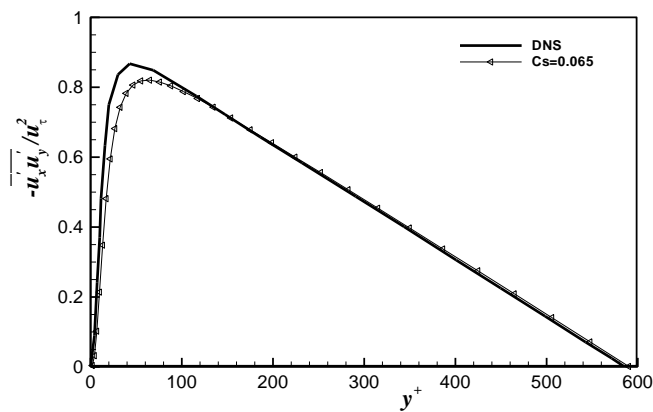


Fig. 5. Reynolds stress profile in wall units.

VII.II. Flow Structures

We have calculated streamwise velocity (\bar{u}_x) distribution at the centerline of the channel and streamwise shear velocity ($\bar{u}_{x\tau}$) distribution at the immediate vicinity of the wall at non-dimensional time, $t = 140.00$. Using these computed data different contour plots of the flow field have been shown. Contour of instantaneous streamwise velocity distribution at the centerline of the channel in x - z plane is shown in Fig. 6. The value of \bar{u}_x ranged between 19.5 and 23.5 in the contour plot. The highest value of \bar{u}_x appears at red regions and lowest value at blue regions in this plot. The higher values of \bar{u}_x appear more densely around the centerline of the channel.

Streamwise Shear Velocity ($\bar{u}_{x\tau}$) can be calculated using (14).

$$\bar{u}_{x\tau} = \sqrt{\frac{\tau_x}{\rho}} \tag{14}$$

where, $\bar{u}_{x\tau}$ = stream wise shear velocity

ρ = density of the fluid

τ_x = stream wise shear stress.

Contour of instantaneous (at $t = 140.00$) streamwise shear velocity ($\bar{u}_{x\tau}$) distribution at the immediate vicinity of the wall of this channel in x - z plane is shown in Fig. 7. The value of $\bar{u}_{x\tau}$ ranged between 0.7 and 2 in this contour plot. The blue streaky structures in the plot represent regions of low shear velocity and the highest value of $\bar{u}_{x\tau}$ is indicated by a red color. The higher values of streamwise shear velocity appear more densely in between the centerline and the wall of this channel.

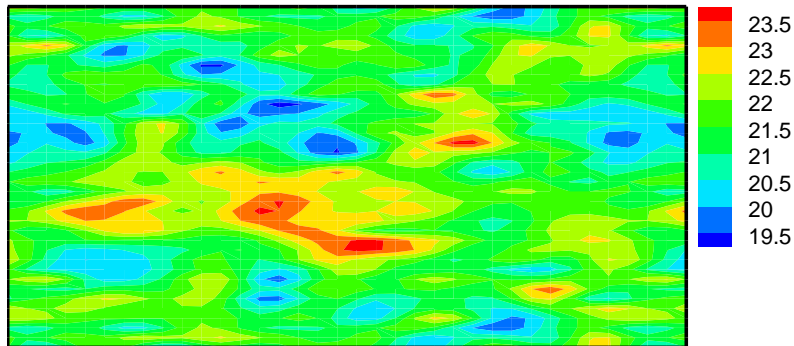


Fig. 6. Contour of streamwise velocity profile in x - z plane.

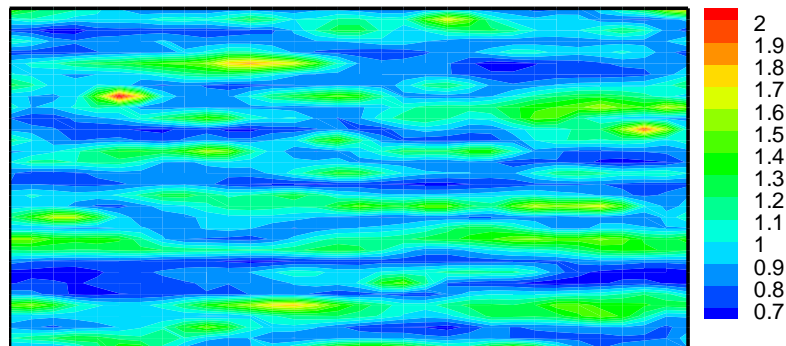


Fig. 7. Contour of streamwise shear velocity profile in x - z plane.

Fig. 8 represents the visualization of vortical structures in the turbulent channel flow by iso-surfaces of the second invariant Q of velocity gradient tensor, which is defined as

$$Q = \frac{1}{2} (\Omega_{ij} \cdot \Omega_{ij} - S_{ij} \cdot S_{ij}) \tag{15}$$

$$\text{where, } \Omega_{ij} = \frac{1}{2} \left(\frac{\partial u_i}{\partial x_j} - \frac{\partial u_j}{\partial x_i} \right) \text{ and } S_{ij} = \frac{1}{2} \left(\frac{\partial u_i}{\partial x_j} + \frac{\partial u_j}{\partial x_i} \right) \tag{16}$$

are respectively the strain-rate and rotation tensors, that is, the symmetric and asymmetric part of the velocity gradient tensor: $A_{ij} = \frac{\partial u_i}{\partial x_j} = \Omega_{ij} + S_{ij}$. The visualized region is the whole calculation domain. The level of the

iso-surface is selected to be $Q = 5$. For this value of Q the vortical structures are significant and are randomly distributed over the turbulent flow field. The vortices generated in between near the wall and near the centerline of the channel are more intense than the ones generated around the centerline of the channel.

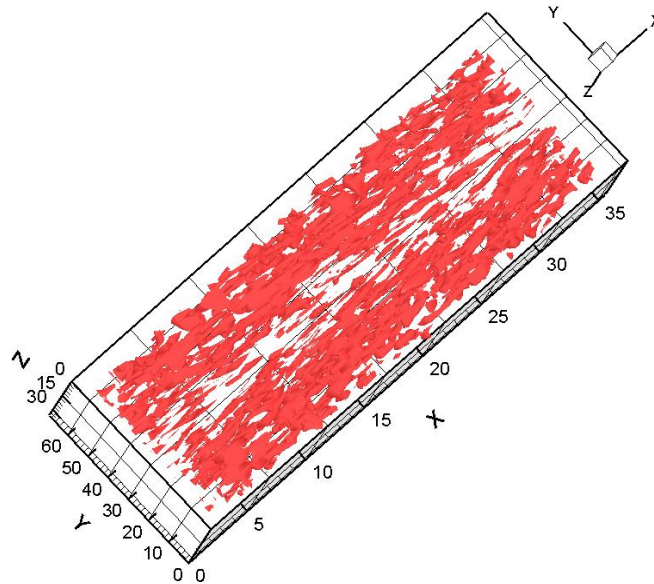


Fig. 8. Iso-surfaces of the second invariant ($Q = 5$) in the channel flow.

VIII. Conclusion

Large eddy simulation in three dimensional plane turbulent channel flow at a low Reynolds number with $32 \times 64 \times 32$ grid points have been successfully performed by using third order low-storage Runge-Kutta method in time and second order finite difference formulation in space. With this Reynolds number the essential turbulence scales have been resolved. The statistical properties show reasonable agreement with the DNS data of reference. Instantaneous streamwise velocity distribution at the centerline of the channel and streamwise shear velocity distribution at the immediate vicinity of the channel flow have also been measured in the contour plot. Visualization of the second invariant ($Q = 5$) in the turbulent channel flow show that the flow field contains lots of coherent tube-like structures which are randomly distributed over the turbulent flow field, and the intensity of the coherent structures is high in between near the wall and the centerline of the channel.

Acknowledgements

This research work is partially supported by the ‘Bangabandhu Fellowship on Science and ICT Project’ which is gratefully acknowledged.

References

- [1]. J. Kim, P. Moin, and R. Moser, Turbulence statistics in fully developed channel flow at low Reynolds number, *Journal of Fluid Mechanics*, 177, 1987, 133-166.
- [2]. R. D. Moser, J. Kim, and N. N. Mansour, Direct numerical simulation of turbulent channel flow up to $Re_\tau = 590$, *Physics of Fluids*, 11(4), 1999, 943-945.
- [3]. J. W. Deardorff, A Numerical study of three-dimensional turbulent channel flow at large Reynolds numbers, *Journal of Fluid Mechanics*, 41, 1970, 453-465.
- [4]. P. Moin, and J. Kim, Numerical Investigation of Turbulent Channel Flow, *Journal of Fluid Mechanics*, 118, 1982, 341-377.
- [5]. F. Yang, H. Q. Zhang, C. K. Chan, and X. L. Wang, Large Eddy Simulation of Turbulent Channel Flow with 3D Roughness Using a Roughness Element Model, *Chinese Physics Letters*, 25 (1), 2008, 191-194.
- [6]. U. Piomelli, P. Moin, and J. E. Ferziger, Model Consistency in Large Eddy Simulation of Turbulent Channel Flows, *Physics of Fluids*, 31, 1988, 1884-1891.
- [7]. U. Piomelli, and E. Balaras, Wall-Layer Models for Large-Eddy Simulations, *Annual Review of Fluid Mechanics*, 34, 2002, 349-374.
- [8]. Z. Xie, B. Lin, and R. A. Falconer, Large-eddy simulation of the turbulent structure in compound open-channel flows, *Advances in Water Resources*, 53, 2013, 66-75.

- [9]. F. E. Ham, F. S. Lien, and A. B. Strong, A Fully Conservative Second-Order Finite Difference Scheme for Incompressible Flow on Nonuniform Grids, *Journal of Computational Physics*, 177, 2002, 117-133.
- [10]. Y. Morinishi, Skew-symmetric form of convective terms and fully conservative finite difference schemes for variable density low-Mach number flows, *Journal of Computational Physics*, 229, 2010, 276-300.
- [11]. B. Sanderse, and B. Koren, Accuracy analysis of explicit Runge-Kutta methods applied to the incompressible Navier-Stokes equations, *Journal of Computational Physics*, 231, 2012, 3041-3063.
- [12]. J. H. Williamson, Low-storage Runge-Kutta schemes, *Journal of Computational Physics*, 35, 1980, 48-56.
- [13]. P. Sagaut, *Large Eddy Simulation for Incompressible Flows: An Introduction* (Berlin Heidelberg: Springer-Verlag, 2001).
- [14]. C. A. Kennedy, M. H. Carpenter, and R. M. Lewis, Low-storage, explicit Runge-Kutta schemes for the compressible Navier-Stokes equations, *Applied Numerical Mathematics*, 35, 2000, 177-219.
- [15]. D. B. Johnson, P. E. Raad, and S. Chen, Simulation of impacts of fluid free surfaces with solid boundaries, *International Journal for Numerical Methods in Fluids*, 19, 1994, 153-176.
- [16]. Y. Morinishi, T. S. Lund, O. V. Vasilyev, and P. Moin, Fully Conservative Higher Order Finite Difference Schemes for Incompressible Flow, *Journal of Computational Physics*, 143, 1998, 90-124.
- [17]. H. K. Versteeg, and W. Malalasekera, *An introduction to computational fluid dynamics* (England: Longman Group Limited, 1995).
- [18]. J. D. Jr. Anderson, *Computational Fluid Dynamics* (New York: McGraw-Hill, Inc., 1995).